A98-31697 ICAS 98-7,3,1

A Simple Analytical Model for Parametric Studies of Hypersonic Waveriders

Ryan P. Starkey *
Department of Aerospace Engineering
University of Maryland, College Park, MD 20742

Abstract

An analytical, power-law derived hypersonic waverider model is developed using a three-dimensional wedge-based flowfield with viscous effects. The model is designed for simple parametric tradeoffs, and understanding of more complex optimization results. This analytical model is validated against a viscous optimized conical waverider created using an inverse design technique. Off-design performance of the analytical model at varying Mach numbers and angles-of-attack is validated using an optimized shock defined waverider (which itself has been validated with an Euler CFD calculation). Both the variable wedge angle waverider and shock defined waverider calculations had the same magnitude of error in comparison to the CFD validation L/D ratios (maximum of 2% difference). The variable wedge angle method calculated the same aerodynamic and geometric properties of higher order methods in orders of magnitude less time.

Nomenclature

A, B, C	=	power-law scaling parameters
D	=	drag
F	=	hypergeometric function
G	=	flight condition function
h	=	height
L	=	lift
ℓ	=	length
M	=	Mach number
m, n	=	power-law exponents
OC	=	osculating cone
P	=	pressure
R	=	thermodynamic constant
S	=	area
T	=	temperature
U	=	velocity magnitude
V	=	volume
VW	=	variable wedge angle method
w	=	width
X, Y	=	L/D functions
x, y, z	=	linear dimensions
α	=	angle of attack
β	=	oblique shock inclination angle
γ	=	ratio of specific heats
δ	=	leading edge inclination angle
η	=	volumetric efficiency
θ	=	vehicle centerline wedge angle
μ	=	viscosity
ξ	=	streamline length
ρ	=	density
σ	=	angle-of-attack constant
τ	=	shear stress
ϕ	=	wedge angle function
Ψ	=	L/D functions

Subscripts

alt	=	altitude
ave	=	average
b	=	value for base surface
c	=	value for compression surface, caret-like
cc	=	concave
cv	=	convex
e	=	property at edge of boundary layer
l	=	value for lower surface
lam	=	laminar
nc	=	non caret-like
p	=	planform
S_p	=	based on planform area
S_s	=	based on the surface area of a sphere
S_w	=	based on wetted surface area
$turb$	=	turbulent
u	=	value for upper surface
V_s	=	based on the volume of a sphere
v	=	viscous
w	=	wall value, wetted surface area
	=	wave drag
∞	=	freestream value or surface

*Graduate Research Assistant, Student Member AIAA.
E-mail: rstarkey@eng.umd.edu

Introduction

A promising concept for the design of high L/D hypersonic vehicles is the "waverider", presented by Nonweiler[1] in 1959. Waveriders are designed so that the bow shock is attached everywhere to the sharp leading edge. As a result of this attached shock, waveriders exhibit very high values of L/D, as shown by theory, experiment[2], and computation[3], although not necessarily the lowest drag. The high lift generated by waveriders is provided by a region of high pressure air which exists between the undersurface and the attached shock.

This paper will explore the aspects of parametric design of hypersonic waveriders using a wedge derived power-law shaped vehicle with either constant or variable spanwise wedge angles. An advantage to these models are their versatility in generating a wide variety of geometries which closely mimic inverse hypersonic vehicle designs, while still retaining the analytical calculation simplicity of the more generic "caret" waveriders, generated from a simple wedge flowfield.

Wedge Derived Flowfield Model

Geometry

A general description of waverider geometries is derived with two-dimensional power-law equations which define the curvature of both the planform and upper surfaces:

$$y_p = Ax^n \tag{1}$$

$$y_u = B(z_u)^n \longrightarrow z_u = \left(\frac{y_u}{B}\right)^{\frac{1}{n}} \tag{2}$$

where the zero coordinate point is at the nose centerline with the height defined as positive going down, as shown in Figure 1. Parameters A and B are positive sizing constants, and exponent n can vary within the range $0 \rightarrow 1$.

To ensure a planar shock (i.e. a wedge derived flowfield) the vehicle must have a constant wedge angle θ. This is achieved by constraining the curvature of the lower surface to follow the equation:

$$\tan\theta = \frac{z_l - \left(\frac{y_u}{B}\right)^{\frac{1}{n}}}{x - \left(\frac{y_p}{A}\right)^{\frac{1}{n}}} \tag{3}$$

Applying Eqn. 1 between $x = 0$ and the desired vehicle length $x = \ell$ along with Eqn. 2 defines the entire vehicle upper surface. Similarly, applying

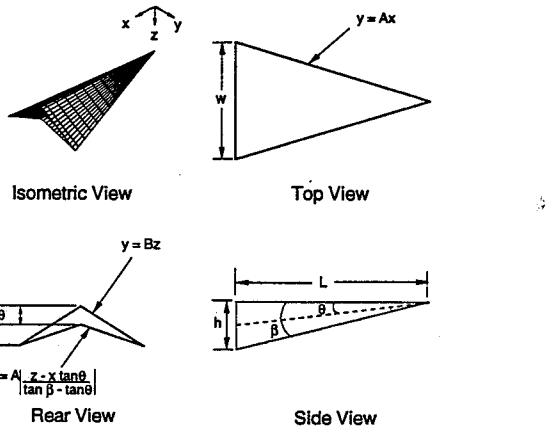

Figure 1: Example of a caret waverider: $A = 0.3$, $n = 1$, $\theta = 5°$, $\ell = 164$ feet

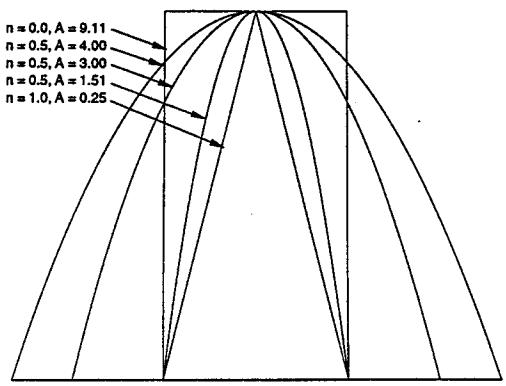

Figure 2: Variations in power-law constant A and exponent n (planform view)

Eqn. 1 between $x = 0$ and the lower surface length, $x = \ell/\cos\theta$, along with Eqn. 3 defines the vehicle lower surface. The vehicle base plane is taken perpendicular to the flight path at a zero degree angle of attack. These equations result in five variables (A, B, n, ℓ, θ) which may be manipulated to generate a wide variety of vehicle configurations.

Small variations of these five parameters can result in large variations in the resulting vehicle geometry, as shown in Figures 2 and 3. At a value of $n = 0$ the vehicle takes on a blunt-planform (spatulate) flat-topped configuration while at $n = 1$ the vehicle is a caret geometry.

Waveriders are designed assuming an attached leading edge shock. Not all variable combinations possible with this parametric geometry will lead to a valid waverider with an attached shock. Shock at-

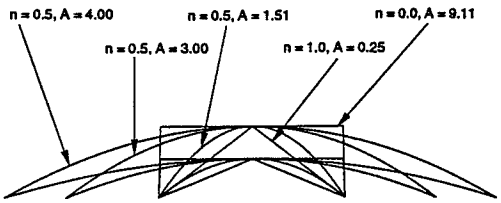

Figure 3: Variations in power-law constant A and exponent n (base view)

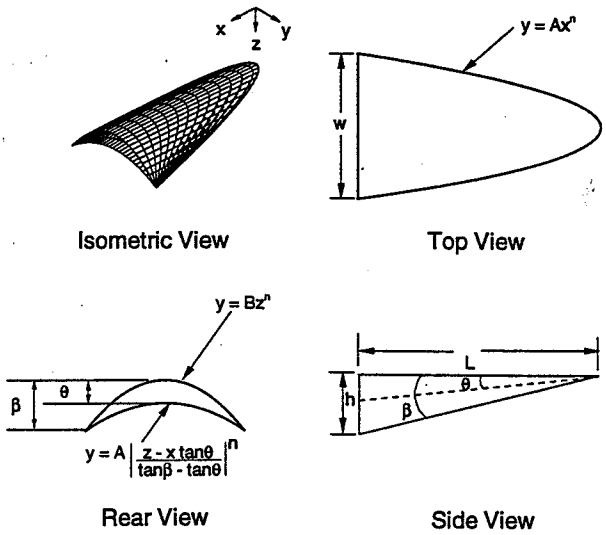

Figure 4: Parametric vehicle example: $A = 0.66$, $n = 0.5$, $\theta = 5°$, $\ell = 164$ feet

tachment is determined by setting:

$$B = \frac{A}{\tan^n \beta} \tag{4}$$

Substituting Eqn. 4 into Eqn. 3 results in:

$$z_l = x \tan\theta + \left(\frac{y_l}{A}\right)^{\frac{1}{n}} (\tan\beta - \tan\theta) \tag{5}$$

for the curvature of the lower surface with an attached shock where β must be less than the maximum shock attachment angle. An example of a vehicle generated using these equations is shown in Fig. 4. The attached shock requirement reduces the number of variable parameters to four: A, n, ℓ, and θ.

This power-law vehicle model is simplistic enough to allow all geometric values to be defined analytically, allowing for quick analysis of different vehicles. The vehicle height h and width w are given by:

$$h = \left(\frac{A}{B}\right)^{\frac{1}{n}} \ell = \ell \tan\beta \tag{6}$$

$$w = 2A\ell^n \tag{7}$$

Using Eqn. 7, the variable parameters can be changed to a more convenient set consisting of ℓ, w, n, and θ.

The planform area of the vehicle S_p is found by integrating the area under the projected leading edge curve, as viewed from above, resulting in:

$$S_p = 2\int_0^{\ell} Ax^n = \frac{w\ell}{n+1} \tag{8}$$

As expected, the planform area of the spatulate vehicle ($n = 0$) is twice that of the caret vehicle ($n = 1$) for constant length and width.

Base area S_b is found from:

$$S_b = 2\int_0^{A\ell^n}\int_{z_u}^{z_l} dz\,dy = S_p \tan\theta \tag{9}$$

Holding the values of w, ℓ, and θ constant and testing n at the two limiting values, shows that the spatulate vehicle ($n = 0$) will have twice the base area of the caret vehicle ($n = 1$).

The volume V for the wedge derived, power-law waverider is:

$$V = 2\int_0^{\ell} S_b(x)\,dx = \frac{S_b\ell}{n+2} = \frac{w\ell^2 \tan\theta}{(n+1)(n+2)} \tag{10}$$

which is more sensitive to changes in the length than the width or wedge angle. Also, the denominator can vary between two (for $n = 0$) and six (for $n = 1$), with the $n = 0$ vehicle having three times the volume of the $n = 1$ vehicle with equal ℓ, w, and θ.

This parametric vehicle allows for many variations in possible configurations by simply changing the value of the power-law exponent n. Also, all of the geometric equations listed reduce to the well-known caret waverider equations[4] at $n = 1$.

The wetted freestream surface area $S_{w\infty}$ and the

wetted compression surface area S_{wc} are:

$$S_{w\infty} = 2\int_0^{\ell}\int_0^{x\tan\beta}\sqrt{1+\frac{A^2n^2z^{2n-2}}{\tan^n\beta}}\,dz\,dx \tag{11}$$

$$S_{wc} = 2\int_0^{\ell}\int_{x\tan\theta}^{x\tan\beta}\sqrt{1+\frac{A^2n^2(z-x\tan\theta)^{2n-2}}{(\tan\beta-\tan\theta)^{2n}}}\,dz\,dx \tag{12}$$

The total wetted surface area of the vehicle is $S_w = S_{w\infty} + S_{wc}$. These may have to be integrated numerically. Alternatively, the summation of the cross products in the vehicle coordinate space provides a fast surface area calculation method.

The volume, wetted surface area, and planform area can then be used to calculate figures of merit, such as the volumetric efficiencies based on wetted surface area η_{S_w} or planform area η_{S_p}, as defined:

$$\eta_{S_w} \equiv V^{\frac{2}{3}}/S_w \tag{13}$$

$$\eta_{S_p} \equiv V^{\frac{2}{3}}/S_p \tag{14}$$

Substituting Eqns. 8 and 10 into Eqn. 14 results in:

$$\eta_{S_p} \equiv \frac{V^{\frac{2}{3}}}{S_p} = \left[\frac{(n+1)}{(n+2)^2}\frac{\ell\tan^2\theta}{w}\right]^{\frac{1}{3}} \tag{15}$$

This shows the small variation in η_{S_p} achievable at the power-law exponent limits of $n = 0$ (spatulate) and $n = 1$ (caret) for constant length, width, and wedge angle to be $\eta_{S_p,n=0} = 1.04\,\eta_{S_p,n=1}$. Therefore, even though there is a large change in volume for changes in n, it comes at the expense of added planform area and scales by about the same margin. For a true gain in η_{S_p} the vehicle should gain all of its volume through height variations (i.e. by increasing θ) and by increasing the length to width ratio. The most efficient exponent n can be found by taking the derivative of η_{S_p} with respect to n and holding ℓ, w and θ constant. This results in $n = 0$ as the exponent which allows for the highest planform efficiency (i.e. spatulate configuration).

Non-conventional figures of merit have been developed to remove what may be perceived as a double accounting of a vehicle's surface area in both the volumetric efficiency and the L/D calculations. This has been done by comparing the vehicle against the properties of a sphere due to the fact that a sphere is the most volumetrically efficient shape possible. Alternate volumetric efficiencies can be based on a comparison to a sphere of equal volume (surface area comparison), η_{S_s}, or a sphere of equal surface area (volume comparison) η_{V_s}:

$$\eta_{S_s} \equiv \frac{(36\pi)^{\frac{1}{3}}V^{\frac{2}{3}}}{S_w} \tag{16}$$

$$\eta_{V_s} \equiv \frac{6\pi^{\frac{1}{2}}V}{S_w^{\frac{3}{2}}} \tag{17}$$

Aerodynamic Performance

Lift and Wave Drag

The flow over the waverider is assumed to be essentially two-dimensional with streamlines flowing straight back over a series of wedges. Lift L and drag due to lift D_L are:

$$L = S_b\sin|\alpha|\,(-1)^{\sigma}[P_b - P_l] + S_p\cos|\alpha|\,[P_l - P_u] \tag{18}$$

$$D_L = S_b\cos|\alpha|\,[P_l - P_b] + S_p\sin|\alpha|\,(-1)^{\sigma}[P_l - P_u] \tag{19}$$

where P_u, P_l, and P_b indicate the pressure for the upper, lower, and base surfaces respectively found using either oblique shock theory or Prantyl-Meyer expansion theory. The parameter $\sigma \equiv 1$ for negative angle of attack, α, and $\sigma \equiv 0$ for $\alpha \geq 0$.

Viscous Drag

Both the laminar and turbulent solutions have been derived using the reference temperature method. In most cases, the transition point will be unknown, so these two results will bracket the actual value. Following the two-dimensional streamline assumption the viscous drag is estimated by integrating along two-dimensional streamlines over the area of the vehicle.

The skin friction for laminar flow $\tau_{w,lam}$ is:

$$\tau_{w,lam} \approx 0.332\,\rho_e U_e^2\sqrt{\frac{C^*}{Re_{x,e}}} \equiv \frac{G_{1,lam}}{2x^{1/2}} \tag{20}$$

where the conditions at the edge of the boundary layer are approximated using post-shock conditions and function $G_{1,lam}$ (defined in Eqn. 20) is shown in Table 1. The parameter C^* is the Chapman-Rubensin parameter evaluated at average boundary-layer conditions[5] and is solved for using the power-law viscosity approximation given by:

$$C^* = \left(\frac{T^*}{T_e}\right)^{n-1} \approx \left(\frac{T^*}{T_e}\right)^{-1/3} \text{ for air} \tag{21}$$

	Laminar Flow	Turbulent Flow
G_1	$0.664\sqrt{\rho_e U_e^3 \mu_e C^*}$	$0.037(U_e)^{1.8}(\rho^*)^{0.8}(\mu^*)^{0.2}$
G_2	0.5	0.8
F_0	0.99845	0.99758
F_1	-0.57529	-0.80941
F_2	0.36737	0.54989
F_3	-0.11939	-0.18247

Table 1: Viscous drag constants for wedge derived waverider

where T^*/T_e is found using Eckert's empirical estimate for the average boundary layer temperature:

$$\frac{T^*}{T_e} \approx 0.5 + 0.039M_e^2 + 0.5\frac{T_w}{T_e} \tag{22}$$

and the wall temperature is estimated depending on the application. For hypersonic vehicles at cruise conditions, a good estimate is $T_w \approx 1100$ K. For this model the wall temperature is assumed to be constant.

Dynamic viscosity μ at the edge of the boundary layer is approximated by Sutherland's law[5].

Laminar viscous drag D_{lam} is then found by integrating the skin friction over the length of a streamline $\xi(y)$ and then over all streamlines for the upper (u) and lower (l) surfaces respectively:

$$D_{lam,u} = G_{1,lam,u} \int_0^{A\ell^n} \int_0^{\xi_u(y)} \frac{dx\,dy}{x^{1/2}} \tag{23}$$

$$D_{lam,l} = G_{1,lam,l} \int_0^{A\ell^n} \int_0^{\xi_u(y)/\cos\theta} \frac{dx\,dy}{x^{1/2}} \tag{24}$$

where $\xi(y)$ is the y-dependent streamline length over the upper surface, given by:

$$\xi_u(y) = \ell - \left(\frac{y}{A}\right)^{\frac{1}{n}} \tag{25}$$

The skin friction for turbulent plate flow $\tau_{w,turb}$ is given by:

$$\tau_{w,turb} \approx \frac{0.0592\rho^* U_e^2}{2(Re^*)^{0.2}} = \frac{0.8G_{1,turb}}{x^{0.2}} \tag{26}$$

where the function $G_{1,turb}$ (defined in Eqn. 26) is shown in Table 1 and,

$$Re^* = \rho^* U_e x/\mu^* \tag{27}$$

$$\rho^* = P/RT^* \tag{28}$$

with R being the specific gas constant for air. The values for T^* and μ^* are found by using Eqns. 22 and Sutherland's law, respectively. Turbulent viscous drag D_{turb} is found by integrating Eqn. 26 in the same manner as above for the upper and lower surfaces:

$$D_{turb,u} = 1.6G_{1,turb,u} \int_0^{A\ell^n} \int_0^{\xi_u(y)} \frac{1}{x^{0.2}}\,dx\,dy \tag{29}$$

$$D_{turb,l} = 1.6G_{1,turb,l} \int_0^{A\ell^n} \int_0^{\xi_u(y)/\cos\theta} \frac{1}{x^{0.2}}\,dx\,dy \tag{30}$$

Since both the laminar and turbulent viscous drag equations are of the same form, they are evaluated in the same manner. The only difference between the equations for the upper and lower surfaces are the integration limits (i.e. $\xi_l(y) = \xi_u(y)/\cos\theta$). Therefore, the same equation can be used for the upper and lower surface since the upper surface is aligned with the freestream flow direction (i.e. using $\theta = 0°$) when evaluated with the proper atmospheric conditions. Integrating by parts in both the x and y directions results in a series solution for the viscous drag D_v, represented by a hypergeometric function of the form:

$$D_v = \frac{G_1 w \ell^{G_2}}{(\cos\theta)^{G_2}} \left(\sum_{k=0}^{\infty} \frac{(n)_k(-G_2)_k}{(1+n)_k} \frac{1^k}{k!}\right) \tag{31}$$

The hypergeometric function can be rewritten as:

$$\sum_{k=0}^{\infty} \frac{(n)_k(-G_2)_k}{(1+n)_k} \frac{1^k}{k!} = \sum_{k=0}^{\infty} \frac{1}{k!} \prod_{p=0}^{k} \frac{(n+p)(p-0.5)}{1+n+p} \tag{32}$$

which fits well to a third order polynomial of the form:

$$F(n) \equiv F_0 + F_1 n + F_2 n^2 + F_3 n^3 \tag{33}$$

for both the laminar and turbulent curves, where F_0, F_1, F_2, and F_3 are constants. This results in the combined laminar and turbulent drag equation for either the upper or lower surface of the vehicle:

$$D_v = G_1 w F(n) \left(\frac{\ell}{\cos\theta}\right)^{G_2} \tag{34}$$

with the constants and functions, F and G, as shown in Table 1. Values in Eqn. 34 are for using SI units. It is easy to see that Eqn. 34 scales linearly with the width, and to the G_2 power of ℓ. Also, the power-law exponent n only appears within the function $F(n)$.

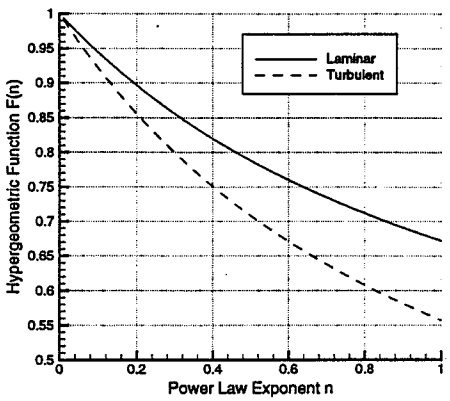

Figure 5: Hypergeometric function $F(n)$ vs. power-law exponent n

Only the implicit functional dependence on θ cannot be readily determined due to the atmospheric properties in the variable G_1.

The plot of the hypergeometric function for both the laminar and turbulent cases is shown in Fig. 5 for variations in the power-law exponent n from zero to one. Eqn. 34 shows that for a constant set of values for ℓ, w, and θ the viscous drag scales by the hypergeometric function. For the laminar case, the viscous drag at $n = 1$ is 67% of the value at $n = 0$. Similarly, at $n = 1$ the turbulent drag is 56% of the $n = 0$ case. Therefore, even though the $n = 1$ vehicle has 33% of the volume and 50% of the planform area of the $n = 0$ vehicle, it has a disproportionately higher amount of viscous drag.

L/D Equation

The lift-to-drag ratio can be derived from the previously defined L and D. Writing Eqns. 18, 19, and 34 in the form of the complete L/D equation:

$$\frac{L}{D} = \frac{L}{D_L + D_v} \tag{35}$$

and then dividing through by $\cos|\alpha|[P_l - P_u]$ and substituting Eqn. 9 into S_b, results in the following simplified L/D equation:

$$\frac{L}{D} = \frac{1}{\Psi_1(\theta,\alpha,M_\infty,h_{alt}) + \Psi_2(\theta,\alpha,M_\infty,h_{alt})\Psi_3(\ell)\Psi_4(n)} \tag{36}$$

where h_{alt} is the design or cruise altitude and,

$$\Psi_1 \equiv \frac{X+Y}{1-XY} \tag{37}$$

$$\Psi_2 \equiv \left(G_{1,u} + \frac{G_{1,l}}{(\cos\theta)^{G_2}}\right) \frac{1}{(P_l - P_u)\cos|\alpha|(1-XY)} \tag{38}$$

$$\Psi_3 \equiv \ell^{G_2 - 1} \tag{39}$$

$$\Psi_4 \equiv (n+1)(F_0 + F_1 n + F_2 n^2 + F_3 n^3) \tag{40}$$

$$X \equiv \tan\theta \left[\frac{P_l - P_b}{P_l - P_u}\right] \tag{41}$$

$$Y \equiv (-1)^\sigma \tan|\alpha| \tag{42}$$

For a given design point Mach number and altitude, the L/D becomes a function of only θ, α, ℓ, and the power-law exponent n. The smaller the denominator in Eqn. 36, the larger the L/D becomes. All viscous effects are contained in the Ψ_2 term, while all length dependence and power-law exponent dependence have been decoupled into the $\Psi_3(\ell)$ and $\Psi_4(n)$ terms, respectively. Both of the functions Ψ_1 and Ψ_2 contain some component of lift of the vehicle through the function X, as well as, the $(P_l - P_u)$ term in Ψ_2.

At $\alpha \approx -\theta/2$, the pressure term $(P_l - P_u)$ in the denominator of Ψ_2 and X goes to zero, but L/D is still defined. Taking the limit as $\alpha \to -\theta/2$, it can be found that Eqn. 36 reduces to:

$$\lim_{\alpha \to -\theta/2} \frac{L}{D} = \frac{-1}{\frac{1}{Y} + \left(G_{1,u} + \frac{G_{1,l}}{(\cos\theta)^{G_2}}\right) \frac{\Psi(n)\Psi(\ell)}{(P_l - P_b)Y\tan\theta\cos|\alpha|}} \tag{43}$$

Note that Eqns. 36 and 43 are independent of the width of the vehicle. This is an inherent characteristic due to the uniform wedge angle of the vehicle and, therefore, the constant flow properties along each streamline. Also, due to the fact that the width scales with the constant A for a given exponent n (i.e. $w = 2A\ell^n$), the width of each streamline scales by the same constant, thereby scaling the viscous drag linearly in A. Using variations in the vehicle's width, the vehicle can be tailored to achieve any desired volume. This allows for incredible flexibility in choosing the design geometry.

Variable Wedge-Angle Vehicle Model

Vehicle Geometry

The derived model can be expanded to include non-planar shocks. The methodology for the generation of this vehicle is the same as the wedge derived vehicle, with the addition of a third power-law function to include lower surface curvature:

$$y_{l,cc} = C(z_{l,cc} - x\tan\theta)^m \longrightarrow z_{l,cc} = \left(\frac{y_{l,cc}}{C}\right)^{\frac{1}{m}} + x\tan\theta \tag{44}$$

for $\theta < \delta$ (i.e. concave (cc) surface) where δ is the angle of the leading edge measured relative to

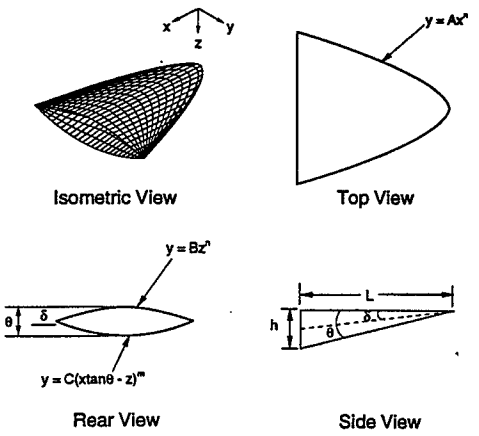

Figure 6: Convex parametric variable wedge angle vehicle example: $A = 2.1$, $m = 0.5$, $n = 0.6$, $\theta = 12°$, $\delta = 6°$, $\ell = 36.58$ m

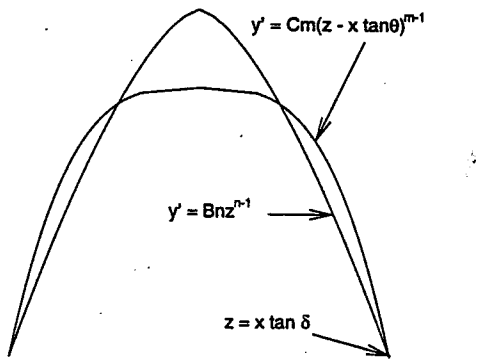

Figure 7: An example of a non-physical combination of variables

freestream, m is a second power-law exponent which can vary between 0 and 1, and C is the lower surface power-law constant. A vehicle with a convex (cv) lower surface has curvature defined by:

$$y_{l,cv} = C(-z_{l,cv} + x\tan\theta)^m \longrightarrow z_{l,cv} = x\tan\theta - \left(\frac{y_{l,cv}}{C}\right)^{\frac{1}{m}} \tag{45}$$

Unlike the planar-shock vehicle, these equations result in six variables (A, n, m, ℓ, θ, δ) which may be manipulated to generate a wide variety of vehicle designs where the upper surface power-law constant is defined as $B = A/\tan^n\delta$. This is very similar to Eqn. 4 where the shock angle β has been replaced by the leading edge angle δ. The introduction of the parameter δ allows for the leading edge angle to be defined independent of the shock angle (which is not constant for this geometry). The parameters C is a scaling factor used to align the leading edges of the upper and lower surfaces:

$$C = \frac{Ax^{n-m}}{|\tan\theta - \tan\delta|^m} \tag{46}$$

Absolute value is used because C must always be positive, regardless of whether vehicle is convex or concave. An example of a convex vehicle generated using these equations is shown in Fig. 6.

This general model produces a planar shock at the specific case of $n = m$. For $n = m = 1$, these equations create the caret style waverider with an attached shock with $\delta = \beta$.

The lower surface cannot cross the upper surface, so the ratio of the slopes at the leading edge:

$$\frac{y'_{l,cc}}{y'_{u,cc}} = \frac{m}{n}\frac{\tan\delta}{\tan\delta - \tan\theta} \tag{47}$$

must be less than unity for the concave vehicle. An example of a shape in which this is not true is shown in Fig. 7. This can be rewritten in terms of the following inequality for small angles with an attached shock:

$$\frac{m}{n}\frac{\delta}{\delta - \theta} > 1 \tag{48}$$

which must be satisfied for a feasible design.

Another way to write Equation 47 is in terms of the minimum wedge angle for a given set of variables:

$$\theta_{cc,min} = \delta\left(1 - \frac{m}{n}\right) \tag{49}$$

Height h, width w, and planform area S_p for the variable wedge angle vehicles are the same as shown in Eqns. 6 through 8 for the vehicle with the wedge derived flowfield. Base area S_b of the variable wedge angle derived vehicles can be found by solving the equations:

$$S_{b,cc} = 2\int_0^{A\ell^n}\int_{z_u}^{z_{l,cc}} dz\,dy \tag{50}$$

$$S_{b,cv} = 2\int_0^{A\ell^n}\int_{z_u}^{z_{l,cv}} dz\,dy \tag{51}$$

where the z-coordinate of the upper surface is found from Eqn. 2 and the z-coordinates for the lower surfaces of the concave and convex geometries are found from Eqns. 44 and 45, respectively. The solution, which is the same for both vehicles, has been divided into two terms, $S_{b,c}$ and $S_{b,nc}$, shown by the

equations:

$$S_{b,c} = S_p \tan\theta \frac{n+1}{m+1} \tag{52}$$

$$S_{b,nc} = S_p \tan\delta \frac{m-n}{m+1} \tag{53}$$

where $S_b = S_{b,c} + S_{b,nc}$. Equation 52 becomes the base area of a caret (c) waverider for $n = m = 1$. Therefore, this term indicates how closely the vehicle corresponds to a caret-like waverider[4]. This leaves the second term to represent the non-caret (nc) waverider base area correction.

The volume V of the variable wedge angle waverider is found from integrating the local base area $S_b(x)$ (i.e. replace ℓ with x in Eqn. 50 or 51) down the length (x) of the vehicle where the solution follows directly as functions of $S_{b,c}$ and $S_{b,nc}$ as shown in the following equation:

$$V = S_b \frac{\ell}{n+2} \tag{54}$$

The equation for volume is the same regardless of whether the vehicle has a concave or convex lower surface.

Surface area calculation for the variable wedge angle derived parametric vehicle requires a simple numerical integration of Equation 11 for the wetted freestream surface area and the following equation for the wetted compression surface area:

$$S_{wc} = 2 \int_0^{\ell} \int_{x\tan\theta}^{x\tan\delta} \sqrt{1 + C^2 m^2 (z - x\tan\theta)^{2m-2}}\, dz\, dx \tag{55}$$

This results in the total wetted surface area of the vehicle equal to $S_w = S_{w\infty} + S_{wc}$.

Aerodynamic Performance

Lift and Drag Due to Lift

For the purposes of this analysis, even with a curved shock, the flow over the waverider is again assumed to be two-dimensional with streamlines flowing straight back over a series of wedges. Since these vehicles do not have uniform spanwise surface angles, the flowfield is solved at each local spanwise angle. This results in what has been termed the variable wedge angle (VW) flowfield. Local spanwise angles ϕ_{local} for either the concave or convex vehicles are solved from:

$$\phi_{local} = \tan^{-1}\left[\frac{\Delta z}{\xi(y)}\right] \tag{56}$$

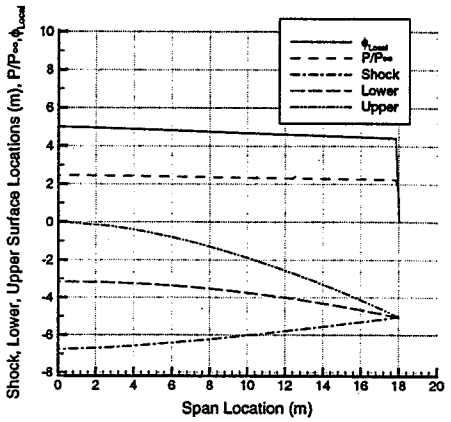

Figure 8: Concave variable wedge angle vehicle exit plane geometry and shock location

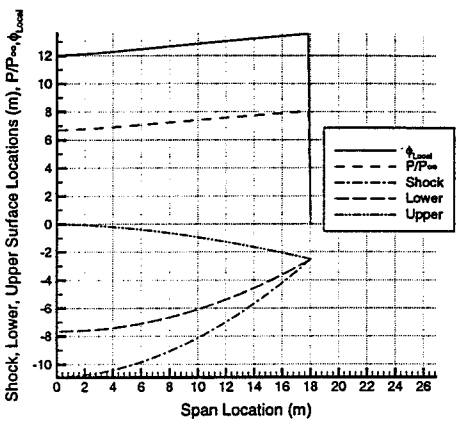

Figure 9: Convex variable wedge angle vehicle exit plane geometry and shock location

where the local vehicle height Δz is given by:

$$\Delta z = \left(\frac{y}{A}\right)^{\frac{1}{m}} (\tan\delta - \tan\theta)\ell^{1-\frac{n}{m}} + \ell\tan\theta - \left(\frac{y}{A}\right)^{\frac{1}{n}} \tan\delta \tag{57}$$

and $\xi(y)$ is solved using Eqn. 25. The variations in the local angle across the half-span of the vehicle, the associated compression surface shock pressure ratio, and the exit plane shock profile are shown in Figures 8 and 9 for the concave and convex vehicles, respectively, where $z_{shock,local} = \xi(y)\tan\beta_{local}$.

Following the same format as the wedge derived waveriders, this method can also easily account for variable angles of attack by using the parameter σ defined for Eqns. 18 and 19. Use of this parameter results in the following lift and wave drag equations

by summing of pressure forces over the body:

$$L = 2\int_0^{A\ell^n} \{\xi(y)[P_l - P_u]\cos|\alpha| + \Delta z(-1)^\sigma[P_b - P_l]\sin|\alpha|\}\, dy \tag{58}$$

$$D_L = 2\int_0^{A\ell^n} \{\xi(y)(-1)^\sigma[P_l - P_u]\sin|\alpha| + \Delta z[P_l - P_b]\cos|\alpha|\}\, dy \tag{59}$$

where P_u, P_l, and P_b indicate the pressures for the upper, lower, and base surfaces respectively. These pressures are solved using either the oblique shock or Prantyl-Meyer relations. A "vehicle-averaged wedge angle" is given by:

$$\phi_{Average} = \frac{2\int_0^{A\ell^n} \phi_{local}\, dy}{w} \tag{60}$$

Viscous Drag

The skin friction for both laminar and turbulent flows are solved in the same manner as shown for the wedge derived vehicle. Since the upper surface is at a constant angle relative to freestream, it can be solved in the same way as the planar shock waverider. When solving for the lower surfaces, the bounds of integration are integrated over the spanwise angle ϕ_{local} instead of the vehicle wedge angle θ. This results in the total vehicle viscous drag equation:

$$D_v = G_{1,u} w \ell^{G_2} F(n) + \int_0^{A\ell^n} \int_0^{\xi_u(y)/\cos\phi_{local}(y)} \frac{1.6 G_{1,l}(\phi_{local}(y))}{x^{1-G_2}}\, dx\, dy \tag{61}$$

where, G_1, G_2 and $F(n)$ are shown in Table 1.

The implicit drawbacks to this method are: 1) the model is assumed to be a true aerodynamic shape with no losses due to engine-airframe integration (a reasonable approximation for this rocket application), 2) all values of lift and drag assume shock attachment to the leading edge (i.e. no pressure leakage), which is not true for all sets of parameters in this method, 3) centrifugal lift has been neglected, 4) center of pressure and moment forces have not been considered, 5) no control surface or trajectory optimization has been included, 6) transverse flow is assumed to be zero, and 7) the wall temperature is assumed to be constant.

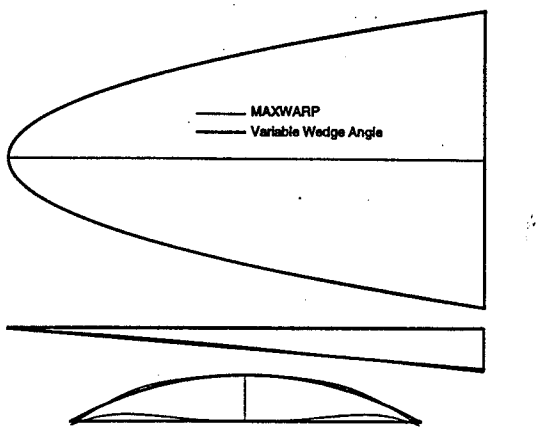

Figure 10: Variable wedge angle comparison geometry with MAXWARP vehicle

Validation Models

The variable wedge power-law waverider model is compared against both conical and osculating cone[6] generated waveriders to validate the methodology.

MAXWARP Conically Derived Waveriders

Using the MAXWARP[7] (Maryland Axisymmetric Waverider Program) optimization code, a suitable conically derived waverider comparison model was generated (a Mach 8 cruiser optimized for maximum L/D).

The planform leading-edge equation ($y = Ax^n$) was curve-fit to the MAXWARP vehicle resulting in values of $A = 2.4566$ and $n = 0.4942$. The resulting variable wedge angle geometry match is shown in Figure 10. As this figure shows, the values of ℓ, w, h, θ, and δ (196.85 feet, 121.91 feet, 16.50 feet, 4.7636°, and 4.7913° respectively) were all held constant between the two vehicles. The freestream Mach number and dynamic pressure were also held constant at 8 and 3821.3 psf.

Specifications are shown in Table 2 for both the MAXWARP vehicle and the resulting variable wedge approximation. The variable wedge vehicle has a 8.3% larger volume and 6.6% larger base area. The outcome was a model which had a 7.2% lower L/D, 3.2% more lift, 2.9% less wave drag, and 53.5% more viscous drag than the MAXWARP vehicle. The discrepancy in the viscous drag is because the MAXWARP program calculate the vehicle's wall temperature profile, whereas the variable wedge vehicle assumes a single constant wall temperature. Therefore, it is clearly shown that the variable wedge

	MAXWARP	V. W.	% Diff.
V (m^3)	2,756	2,984	8.30
S_w (m^2)	3,051	3,032	-0.63
S_p (m^2)	1,496	1,492	-0.25
S_b (m^2)	117	124	6.61
η_{S_s}	0.3115	0.3307	6.16
η_{S_p}	0.1314	0.1389	5.71
L/D	8.44	8.32	-1.42
L ($\times 10^6$ N)	7.990	8.385	4.94
D_w ($\times 10^6$ N)	0.707	0.699	-1.11
D_v ($\times 10^6$ N)	0.240	0.309	28.7

Table 2: Variable wedge angle model validation with MAXWARP vehicle

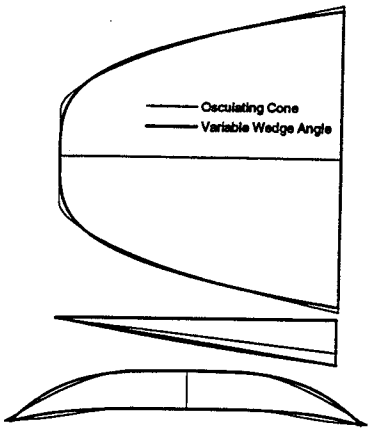

Figure 11: Variable wedge angle planform curve fit comparison geometry with osculating cone vehicle

model is able to simply and analytically solve for the same characteristics which take orders of magnitude more time to solve using the conical method.

Osculating Cone Derived Waveriders

The method of osculating cones [6] is an infinite degree of freedom tool used for inverse waverider design. Using models generated by Takashima [8] with this method, a comparison was made to validate off-design performance for different Mach numbers and angles of attack. Takashima validated the method of osculating cones using an inviscid CFD calculation of the optimized Mach 10 vehicle shown in Figure 11. The vehicle approximation was made using the variable wedge angle method by curve-fitting ($y = Ax^n$) to the planform surface of the osculating cone generated waverider. The vehicle approximation is fairly close to the desired shape with only slight differences in the resulting geometries. They were matched to have equal length, width, height, and centerline and leading edge angles of 22.12 m, 24.16 m, 3.50 m, 6.56°, and 9.00° respectively.

The comparisons to the off-design CFD calculations are shown for Mach numbers between 4 and 10 and angles of attack between -6° and 6° are shown in Table 3. Data is given for the lift, inviscid drag, and L/D for the CFD osculating cone and analytical variable wedge angle calculations. All results agree with the CFD validation numbers other than for the $\alpha = -4°$ cases. The error for these cases is 20% since this angle is close to the vehicle's zero lift angle of about 3.3° (i.e. low magnitude of lift results in a large error with small departures from the solution). Coincidentally, the variable wedge angle and osculating cone methods had the same magnitude of errors (maximum difference was at $\alpha = -4°$ and was 2.4%) in comparison to the CFD calculation, although the variable wedge angle method is orders of magnitude faster to calculate. This makes the variable wedge angle method extremely powerful for parametric studies of hypersonic waveriders.

Conclusions

Use of a parametric vehicle will allow for quick analytical studies to help determine a first order approximation for a desirable vehicle configuration. Towards this goal, two different power-law derived vehicle models have been developed. The first is a strictly planar-shock geometry with four variable generating parameters, the second model contains six parameters and can therefore be fit to more realistic configurations. Due to the three-dimensional nature of the second model, a variable wedge angle analysis has been developed. This method has been validated using both conically and osculating cone derived waveriders. The variable wedge angle method has been shown to have the same accuracy as the osculating cone method for an optimized waverider configuration, thereby making the variable wedge angle method extremely powerful for parametric studies of hypersonic waveriders. Also, since the planar shock model is contained as a subset of the variable wedge angle model (i.e. fewer parameters) it allows for even greater insight into the characteristics of these type of vehicles.

		Lift ($\times 10^5$N)			Drag ($\times 10^5$N)			L/D		
M_∞	α	O. C.	V. W.	% Error	O. C.	V. W.	% Error	O. C.	V. W.	% Error
4	0°	14.62	15.01	2.67	3.632	3.716	2.30	4.03	4.04	0.36
6	0°	11.08	11.15	0.68	2.145	2.162	0.77	5.16	5.16	-0.09
8	0°	9.356	9.377	0.22	1.566	1.570	0.28	5.97	5.97	-0.06
10	0°	8.379	8.441	0.73	1.276	1.286	0.74	6.57	6.57	0.00
10	-6°	-6.194	-6.945	12.12	1.013	1.095	8.10	-6.11	-6.34	3.72
10	-4°	-1.443	-1.813	25.65	0.675	0.705	4.39	-2.14	-2.57	20.36
10	-2°	3.344	3.239	-3.13	0.757	0.767	1.27	4.42	4.22	-4.35
10	0°	8.379	8.441	0.73	1.276	1.286	0.74	6.57	6.57	0.00
10	2°	13.84	14.01	1.20	2.274	2.294	0.86	6.09	6.11	0.34
10	4°	19.87	20.10	1.20	3.813	3.849	0.95	5.21	5.22	0.25
10	6°	26.53	26.84	1.16	5.968	6.027	0.99	4.45	4.45	0.17

Table 3: Variable wedge angle model off-design Mach number and angle-of-attack validation data

Future Work

Since the variable wedge angle model is analytical and the results are the same as both the conical and osculating cone vehicles, an optimizer could arrive at the same solutions as the validation models with significantly less time using the variable wedge model.

This parametric tool is also currently being used to investigate multiple classes of waverider vehicles for Boeing[9] to determine the trade-offs associated with hypersonic vehicle design.

Acknowledgments

This research was supported by the Center for Hypersonic Education and Research at the University of Maryland under technical monitor Dr. Isaiah Blankson of NASA (NASA grant #NAGw 11796), as well as by the Boeing Space Transportation Concepts and Analysis Business Development Division under technical monitor Dr. Dana Andrews (Boeing contract #JQ4085), the support of whom is greatly appreciated. Thanks also go to all students, past and present, at the University of Maryland Center for Hypersonic Education and Research who contributed to this work.

References

[1] Nonweiler, T. R. F., "Aerodynamic Problems of Manned Space Vehicles," *Journal of the Royal Aeronautical Society*, Vol. 63, 1959, pp. 521–528.

[2] Gillum, M. J. and Lewis, M. J., "Experimental Results on a Mach 14 Waverider with Blunt Leading Edges," *Journal of Aircraft*, Vol. 34, May-June 1997, pp. 296–303.

[3] Takashima, N. and Lewis, M. J., "Navier-Stokes Computation of a Viscous Optimized Waverider," *AIAA Paper 92-0305*, 1992.

[4] Rasmussen, M., *Hypersonic Flow*. New York, NY: Wiley-Interscience, 1994.

[5] White, F. M., *Viscous Fluid Flow*. New York: McGraw-Hill, first ed., 1974.

[6] Sobieczky, H., Dougherty, F. C., and Jones, K., "Hypersonic Waverider Design from Given Shock Waves," *Proceedings of the First International Hypersonic Waverider Symposium*, University of Maryland, College Park Oct. 17-19, 1990.

[7] Corda, S. and Anderson, J. D., "Viscous Optimized Hypersonic Waveriders Designed From Axisymmetric Flowfields," *AIAA Paper 88-0369*, Jan 1988.

[8] Takashima, N., *Optimization of Waverider Based Hypersonic Vehicle Designs*. PhD thesis, University of Maryland, May 1997.

[9] Starkey, R. and Lewis, M. J., "A Parametric Study of L/D and Volumetric Efficiency Trade-Offs for Waverider Based Vehicles," Boeing Space Transportation Concepts and Analysis Business Development Division, February 1998.